Breaking wave impact on a floating body with air bubble effect

Shiyan Sun, Guoxiong Wu*, Gang Xu

School of Naval Architecture and Ocean Engineering, Jiangsu University of Science and Technology, Zhenjiang, 212003, China

Abstract:

The hydrodynamic problem of a breaking wave impacting on a floating body with air bubble effect is modelled based on the incompressible velocity potential theory, which is solved using the boundary element method in the time domain. To avoid the numerical inaccuracies due to the sharp temporal and spatial variations of velocity and pressure at the initial stage of impact, a dual system is adopted. The simulation close to the impact zone is conducted in a stretched coordinate system, while away from the impact zone the deformation and propagation of incoming overturning wave is simulated in the physical coordinate system. The continuities of both pressure and velocity are enforced at the interface of two zones. When the impact zone is no longer small, the dual systems will be merged and the simulation will be undertaken in one single domain. The air bubble trapped between the breaking wave and the solid surface is taken into account based on the assumption that the trapped air undergoes an adiabatic process. An auxiliary function method is used to decouple the nonlinear mutual dependence of fluid loading, body motion and bubble deformation. Simulations are undertaken for cases related to breaking wave impact in various engineering problems, including a solid coastal wall, a freely floating ship cross section, a floating breakwater and a tension leg platform. Detailed results for pressure, free surface profile, bubble deformation and body motion are provided, and their physical implications are discussed.

Keywords: breaking wave impact; trapped air bubble; floating body; dual coordinate systems; auxiliary function method; boundary element method.

1. Introduction

The breaking wave is a spectacular phenomenon in the sea. It evidently occurs when there are cyclones, storm surges, tsunami, etc., but it also occurs in mild sea conditions, for example, when a wave meets an obstacle in its path or interacts with other waves. Impact by the breaking wave can pose a great risk to a structure in the ocean, such as a ship, an offshore platform and a breakwater, due to impact produced high loading on the structure. In extreme conditions, a ship may capsize or break, a platform and breakwater can be damaged. Thus the safety, reliability as well survivability of an ocean structure in such a scenario are some of the major concerns in design.

Fluid flow characteristics, including the spatial distribution and temporal variation of velocity, pressure, free surface, during the breaking wave impact are highly complex. When a wave front hits a solid structure, its path is suddenly blocked. The flow direction has to turn sharply, which means a very large acceleration and therefore a very large pressure gradient. The physical process of wave front impact has been demonstrated by Bagnold (1939), Nagai (1961) and Cooker and Peregrine (1995). Various methods have been developed to account for this physical process. Tanizawa and Yue (1992) assumed that the solid surface was 'invisible' to the liquid when the wave front arrived

* Corresponding author. Permanent address: Department of Mechanical Engineering, University College London, Torrington Place, London WCIE 7JE, UK. Tel.: +44 20 7679 3870; fax: +44 20 7388 0180.

E-mail address: g.wu@ucl.ac.uk (G.X. Wu)

at the wall, and the wave would pass the invisible body without any hindrance. Only when the area between the two intersection points of the wall with the undisturbed wave was not small, it would then be taken as the initial wetted surface, and the impact would start at this moment. Zhang et al. (1996) treated the initial impact stage as a self-similar problem. The wave front was approximated as an asymmetric liquid wedge, and the impact velocity was assumed to be a constant and perpendicular to the wall. The wave profile away from the impact was assumed to vary exponentially. Wu (2007a) used a stretched coordinate system method for wave front impact on a wall, and Wu (2007b) subsequently considered the impact by a large liquid droplet on a wall and on a solid wedge. Duan et al. (2009) considered the impact of a wedge shaped wave front on the corner of a coastal wall. The present work considers a two dimensional (2D) breaking wave impact on a floating body or fixed coastal wall. When the section of the structure does not change rapidly, for example near middle section of a slender ship, the two dimensional approximation can be used for impact in the beam sea, similar to the strip theory for ship motion. The result of the 2D theory is expected also to shed some insights into the general 3D problems.

It is generally accepted that the kinetic properties of fluid, especially impact velocity, is the most influential factor for the process of breaking wave impact during impingement onto a structure. However, many scholars have also demonstrated that the entrapped air cavity plays a significant role as well in the physical process of breaking wave impact. The effect of the trapped air pocket was included. The air pocket was assumed to undergo rapid contraction and expansion, and therefore pressure and volume would change adiabatically. An early work is that by Bagnold (1939), in which a wave tank experiment was undertaken. He found that the shock pressure of a thin air pocket was much larger than that of a thick pocket, and when the thickness of air cushion exceeded half of its height, the shock pressure could be neglected. Hattori et al., (1994) investigated the effect of air bubble on wave impact pressure through an experiment. It was observed that the impact pressure with air bubbles was much larger than that without air bubbles. They also found that the characteristics of impact pressure were closely related to the trapped air bubble. The magnitude and frequency of pressure oscillation for the case of the thin pocket being trapped by the breaking wave were much larger than those corresponding to the thick air pocket. When the thick air pocket was trapped, the pressure measured from the sensor would reach a peak rapidly, and after that, it would oscillate with a decreasing amplitude due to the air pocket pulsation. Other typical experimental work on breaking impact includes those by Blackmore and Hewson (1984), Bullock et al. (2001), and Peregrine (2003).

Earlier work on breaking wave impact is based on various approximations, such as Wagner theory (Wagner, 1932) and the method of matched asymptotic expansions (Cointe and Armand, 1987). These approximation methods have been effective for many engineering problems. However, there are also various limitations. A more recent work is that by Song (2015). She used the velocity potential theory with fully nonlinear boundary conditions on the deforming water surface. The trapped air bubble effect and its deformation with time were included based on the assumption of an adiabatic process. A dual coordinate system method was used. The stretched system (Wu, 2007a) was used in a small area of the impact zone at the initial stage to account for the rapid temporal and spatial variation, and physical system was adopted away from the impact zone. Continuity conditions for pressure and velocity were enforced at the interface of two regions. Simulations were undertaken for impact on a fixed wall with air bubble effect.

There are other related works on breaking wave impact using both experiment and numerical

simulations. Manjula et al. (2015) examined the response of a slender vertical cylinder under breaking wave loading by a series of model experiments. The cylinder was fixed at the top but was left free on the bottom. Other experimental work includes those by Ma and Li (2002) for the impact on vertical cylinders in shallow water, Stanczak and Oumeraci (2012) on the surface erosion of a dike slope, and by Hu et al. (2017) on the truncated wall in a wave flume. Computational fluid dynamics (CFD) techniques have also played an important role in dealing with breaking impact with large deformations of free surface and air bubble. Bredmose et al. (2015) investigated the scaling and aeration effects on violent breaking water impacts with trapped air based on compressible-flow theory. Choi et al. (2015) solved the modified Navier-Stokes equations with wave reaction force and dissipation term in a dissipation zone to investigate breaking wave impact forces on a vertical cylinder and two inclined cylinders. Kamath et al. (2016) simulated the breaking wave impact, induced by the variation of water depth, on a slender cylinder in a three-dimensional numerical wave tank based on the open source CFD model.

The above studies have significantly advanced our understanding regarding the characteristics of breaking wave impact. However, much of work with air bubble is for a fixed body. In fact, it is more common for wave to impact on a floating body which moves under the wave excitation. Some new physical features may arise due to body motion, which leads to some new challenges in the numerical simulation. A particular feature is that the breaking wave impact loading, the motion and deformation of bubble and its corresponding pressure oscillation are fully and nonlinearly coupled. In present work, we shall develop a two dimensional numerical technique for breaking wave impact on a floating body with air bubble. The incompressible velocity potential theory is used for the liquid flow. The neglected compressibility may be important for a very short period of time (Khabakhpasheva and Wu, 2007). However, during this period the momentum exchange from wave to body is relatively small for cases which we consider, and therefore the compressibility effect of liquid can be ignored. Fully nonlinear boundary conditions are adopted on the deforming free surface and bubble surface, which are tracked by the time stepping method. At each time step, the velocity potential problem is solved by the boundary element method (BEM). The dual coordinate systems (Song, 2015) are adopted at the early stage of impact. The auxiliary function method (Wu and Eatock Taylor, 2003) is used to decouple the nonlinear mutual dependence of fluid loading, body motion and bubble deformation. The method and numerical procedure are verified through the convergence study and comparison for wave impact on a fixed body, reflecting a coastal wall. Extensive numerical results are provided in various case studies, to account for some typical features related to a freely floating ship, a floating breakwater constrained by nearly horizontal cables and a TLP constrained by two vertical tendons. Results are analysed and their physics associated with breaking wave impact on floating bodies are discussed.

2. Mathematical model and numerical procedure

2.1. Governing equation and boundary conditions

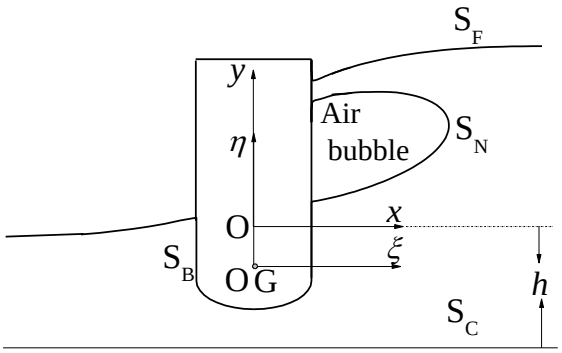

Fig. 1. The sketch of the problem.

The problem is depicted in Fig. 1 which shows an overturning wave impacting on a floating body. When the wave meets the body, an air bubble may be trapped between the body surface S_B and the inner free surface S_N. The outer free surface which is open to air is denoted as S_F. A Cartesian coordinate system $O-xy$ fixed in space is defined in which x-axis coincides with the still water level at $-\infty$ and y-axis points upwards. A body fixed system $O-\xi\eta$ is defined so that the origin is fixed at the rotating centre and ξ-axis and η-axis are perpendicular to and parallel with the central line of body respectively. The water density ρ, the acceleration due to gravity g and water depth h are used for non-dimensionalization. After non-dimensionalization, the horizontal and vertical velocities at the centre of gravity G which is taken as the rotational centre are denoted as U and W respectively, and the rotational velocity about G is Ω. When the fluid is assumed to be incompressible and inviscid, and the flow to be irrotational, the velocity potential ϕ whose gradient is equal to the fluid velocity can be introduced.

The analytical solution of incoming breaking wave is taken from the Airy wave model. Based on the hypothesis of long wave in shallow water, the horizontal velocity $\bar{u}(x)$ averaged along the vertical direction can be written as (Cooker and Peregrine, 1990)

$$\bar{u}(x) = -\frac{1}{2}u_0\{1+\tanh[\nu(x-x_0)]\} \tag{1}$$

This gives a velocity $-u_0$ at $x=\infty$ and zero at $x=-\infty$. x_0 in the equation denotes the initial wave centre with the largest velocity and ν is the parameter which controls the slope of the incoming wave at the initial stage at $x=x_0$. Based on the Airy wave theory, the initial wave profile can be written as (Cooker and Peregrine, 1990)

$$y = f(x) \tag{2}$$

where $f(x) = -\bar{u}(x) + \frac{1}{4}\bar{u}(x)^2$, which varies from zero at $x=-\infty$ to $\Delta h = u_0 + \frac{1}{4}u_0^2$ at $x=\infty$, see Fig. 2. The velocity potential ϕ_I averaged along the vertical direction between the free surface and the bed of the incident wave can be obtained through the integration of the velocity $\bar{u}(x)$ along x direction, and thus we have

$$\phi_I(x)=\int_{x_0}^{x}\bar{u}(x)dx=-\frac{1}{2}u_0\left[x-x_0+\frac{\ln(\cosh\nu(x-x_0))}{\nu}\right] \tag{3}$$

When x_0 is sufficiently far away from the body, the initial wave elevation and the total velocity potential on the surface can be obtained from Eqs. (2) and (3). Subsequently, the free surface elevation will change and velocity will be disturbed. They should be obtained from the solution of the governing equation with the fully nonlinear boundary conditions.

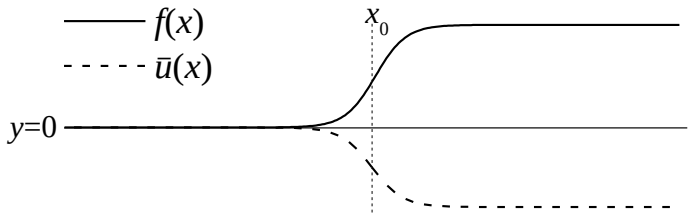

Fig. 2 The sketch of the initial wave profile

Within the whole fluid domain, the total potential ϕ which includes the incident and disturbance potentials satisfies the Laplace's equation

$$\nabla^2\phi=0 \tag{4}$$

Assuming that the trapped bubble undergoes an adiabatic process, the pressure inside the bubble can be expressed as

$$P=P_0(\frac{V_0}{V})^{\gamma} \tag{5}$$

where V_0 is the volume of air bubble when it is first trapped by an overturning wave, V is the volume which varies with time after the moment of impact, and γ is the heat ratio of air. The volume V can be calculated through the integration of discrete nodes constituting the surface of air bubble. Combining Bernoulli equation with the adiabatic process inside the bubble and ignoring the surface tension, the dynamic boundary condition on the inner surface S_N takes the form

$$\frac{D\phi}{Dt}=\frac{1}{2}\nabla\phi\cdot\nabla\phi+\frac{1}{2}u_0^2-(y-\Delta h)-P_0\left[(\frac{V_0}{V})^{\gamma}-1\right] \tag{6}$$

where $D\phi/Dt$ is the material derivative by following a fluid particle in the Lagrangian sense, which is expressed with the symbol D. The dynamic boundary condition on the outer free surface S_F with the constant atmospheric pressure P_0 can be written as

$$\frac{D\phi}{Dt}=\frac{1}{2}\nabla\phi\cdot\nabla\phi+\frac{1}{2}u_0^2-(y-\Delta h) \tag{7}$$

The kinematic boundary conditions on both S_F and S_N in the Lagrangian form can be written as

$$\frac{Dx}{Dt}=\frac{\partial\phi}{\partial x},\quad \frac{Dy}{Dt}=\frac{\partial\phi}{\partial y} \tag{8}$$

The impermeable boundary condition on the body surface takes the form

$$\frac{\partial \phi}{\partial n} = \mathbf{V} \cdot \mathbf{n} = Un_x + Wn_y + \Omega(Xn_y - Yn_x) \tag{9}$$

in which $(X,Y) = (x - x_G, y - y_G)$ is the position vector measured from the rotating centre (x_G, y_G) defined in the frame $O - xy$, $\mathbf{V} = (U - \Omega Y, W + \Omega X)$ is the velocity vector, and $\mathbf{n} = \left(n_x, n_y\right)$ is the normal of surface pointing out of fluid domain. The boundary condition on the seabed can be given as

$$\frac{\partial \phi}{\partial n} = 0 \tag{10}$$

At the far field, where the disturbance is assumed to have diminished and there is only the incoming wave, the boundary condition can be given as

$$\begin{cases} \dfrac{\partial \phi}{\partial x} = 0, & x \to -\infty \\ \dfrac{\partial \phi}{\partial x} = -u_0, & x \to \infty \end{cases} \tag{11}$$

In practical simulations, the computational domain is truncated through a vertical boundary on each side of the body. It is chosen sufficiently away from the body to ensure that the disturbance of the body has not been reflected by the truncated boundary to affect the results near the body surface. Based on the Laplace's equation and the above boundary conditions together with the initial condition, the fluid/structure interaction problem can then be solved through the boundary element method (BEM) combined with a time matching scheme.

2.2. A local stretched coordinate system method for initial impact stage

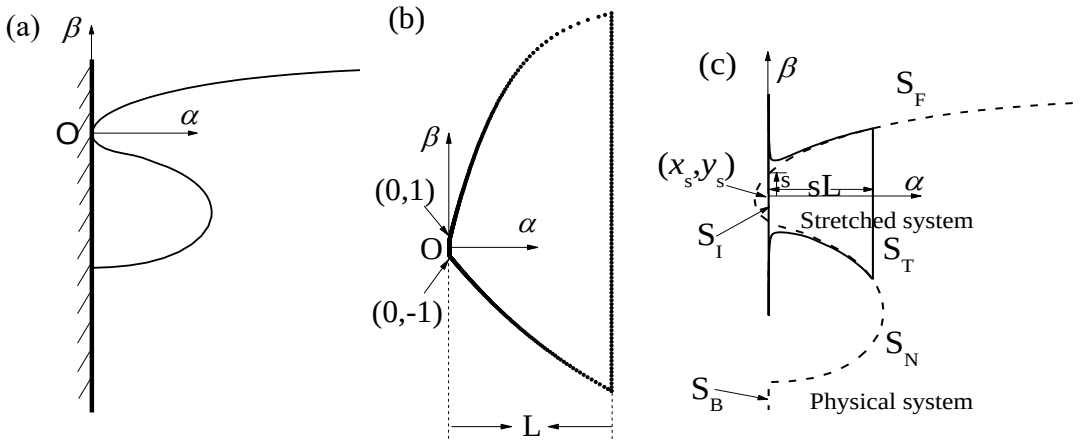

Fig. 3. Sketch for overturning wave impacting on a floating body with infinite height (a) the wave profile at the moment of impact in physical system (b) the initial wave profile with the discretization in the stretched system and (c) the matching between the physical and stretched system.

When the wave front hits the body surface, the contact will normally start from a single point and

then the wetted surface will increase rapidly. During this process, the local physical parameters such as pressure and velocity may experience sharp variation both temporally and spatially. To avoid numerical difficulties due to the extremely small wetted area at the initial stage, which requires extremely small elements to account for the large variation of physical parameters, a stretched coordinate system may be adopted within the impact zone. This has already been used previously in the water entry problem of a wedge (Wu et al., 2004, Sun et al., 2015, 2016). However a major difference is that in the previous work, the condition at the outer boundary is explicitly known. For example, in the case of wedge entering into calm water, the fluid at the outer boundary is assumed to be undisturbed. Here, the outer boundary of the stretched system is the incoming overturning wave which is simulated in the normal physical coordinate system. Therefore the solutions from the two different systems should be properly matched to enforce the flow and pressure continuity conditions.

A stretched coordinate system $O\text{-}\alpha\beta$ is defined with the origin at $(x, y) = (x_s, y_s)$ which is the point where the wave front first touches the body surface. α is in the normal direction of the body surface and β in the tangential direction (see Fig. 3). Without loss of generality, we assume that at the moment of impact α is in the direction of x. The stretched system $O\text{-}\alpha\beta$ together with its origin (x_s, y_s) moves with the body at the horizontal velocity U, the vertical velocity W and the rotational velocity Ω about the rotating centre G. At the moment of impact, the point (x_s, y_s) can be transformed as

$$\xi_{\mathrm{p}} = [(x_s - x_{\mathrm{G}})\cos\gamma + (y_s - y_{\mathrm{G}})\sin\gamma] \tag{12}$$

$$\eta_{\mathrm{p}} = [-(x_s - x_{\mathrm{G}})\sin\gamma + (y_s - y_{\mathrm{G}})\cos\gamma] \tag{13}$$

In the frame moving with the body defined above Eq. (1), $(\xi_{\mathrm{p}}, \eta_{\mathrm{p}})$ is subsequently time independent. We then define

$$s\alpha = [(x - x_{\mathrm{G}})\cos\gamma + (y - y_{\mathrm{G}})\sin\gamma] - \xi_{\mathrm{p}} \tag{14}$$

$$s\beta = [-(x - x_{\mathrm{G}})\sin\gamma + (y - y_{\mathrm{G}})\cos\gamma] - \eta_{\mathrm{p}} \tag{15}$$

$$s\varphi = \phi \tag{16}$$

where the stretching ratio $s(t)$, which varies with time, is set as the half width of intersection line between incident wave crest and body surface, assuming that the incident wave would keep plunging as if it did not touch the wall (see Fig. 3(c)). At the moment of impact, $s(t)$ is equal to the initial stretching ratio s_0. In Eqs. (14) and (15), the displacement of the centre of gravity G can be expressed as

$$q_x(t) = \int_0^t U(\tau)d\tau \tag{17}$$

$$q_y(t) = \int_0^t W(\tau) d\tau \tag{18}$$

and the rotating angle γ can be obtained through

$$\gamma(t) = \int_0^t \Omega(\tau) d\tau \tag{19}$$

Based on Eqs. (14) and (15), we have

$$\varphi_\alpha = \phi_x \cos\gamma + \phi_y \sin\gamma \tag{20}$$

$$\varphi_\beta = -\phi_x \sin\gamma + \phi_y \cos\gamma \tag{21}$$

The temporal derivatives of Eqs. (14) and (15) can be given as

$$\frac{Ds\alpha}{Dt} = [(\frac{Dx}{Dt} - U)\cos\gamma + (\frac{Dy}{Dt} - W)\sin\gamma] + \Omega[-(x - x_G)\sin\gamma + (y - y_G)\cos\gamma] \tag{22}$$

$$\frac{Ds\beta}{Dt} = [-(\frac{Dx}{Dt} - U)\sin\gamma + (\frac{Dy}{Dt} - W)\cos\gamma] - \Omega[(x - x_G)\cos\gamma + (y - y_G)\sin\gamma] \tag{23}$$

Substituting Eqs. (14), (15), (20) and (21) into Eqs. (22) and (23), the kinematic boundary conditions in the stretched system can be transformed as

$$\frac{Ds\alpha}{Ds} \cdot \frac{Ds}{Dt} = \varphi_\alpha - U\cos\gamma - W\sin\gamma + \Omega(s\beta + \eta_p) \tag{24}$$

$$\frac{Ds\beta}{Ds} \cdot \frac{Ds}{Dt} = \varphi_\beta + U\sin\gamma - W\cos\gamma - \Omega(s\alpha + \xi_p) \tag{25}$$

Substituting Eqs. (14), (15), (20) and (21) into the dynamic boundary conditions (6) and (7), we have on the inner surface

$$\begin{aligned} \frac{Ds\varphi}{Ds} \cdot \frac{Ds}{Dt} = {} & \frac{1}{2}\nabla\varphi \cdot \nabla\varphi + \frac{1}{2}u_0^2 - [y_G + (s\alpha + \xi_p)\sin\gamma + (s\beta + \eta_p)\cos\gamma - \Delta h] \\ & - P_0\left[(\frac{V_0}{V})^\gamma - 1\right] \end{aligned} \tag{26}$$

and on the outer free surface

$$\frac{Ds\varphi}{Ds} \cdot \frac{Ds}{Dt} = \frac{1}{2}\nabla\varphi \cdot \nabla\varphi + \frac{1}{2}u_0^2 - [y_G + (s\alpha + \xi_p)\sin\gamma + (s\beta + \eta_p)\cos\gamma - \Delta h] \tag{27}$$

The increase rate $ds/dt = 0.5\phi_n / n_y$, where ϕ_n and n_y are taken from the free surface at the intersection point between the undisturbed incoming wave and the body surface. Based on the consideration that the size of impact zone is proportional to s and the effect of the impact decays exponentially away from the body (Wu, 2001), the domain in the stretched system may be truncated at $\alpha = L$. At this truncated boundary S_T, the disturbance potential is assumed to have sufficiently decayed, and there is only the incident potential. Thus we have

$$\frac{\partial\varphi}{\partial n} = \frac{\partial\phi_I}{\partial n} \tag{28}$$

It should be noted that the normal direction of the truncated boundary in Eq. (28) are taken in the stretched and Cartesian coordinate systems respectively, and they are both pointing out of the fluid

domain of the stretched coordinate system. $\frac{\partial \phi_I}{\partial n}$ on the right hand side of Eq. (28) is taken based on the assumption that the incident wave will propagate forward without the presence of body, and its normal derivative can be obtained through the linear interpolation through $\nabla \phi_I$ in the upper and lower free surfaces.

2.3. The boundary element method

The boundary element method (BEM) is used to solve the above boundary value problems for velocity potential as well the auxiliary functions defined later. Through Green's identity, the Laplace's equation in the fluid domain can be converted into an integral equation over the whole boundary.

$$A(p)\phi(p) = \int (\ln r_{pq} \frac{\partial \phi(q)}{\partial n_q} - \phi(q) \frac{\partial \ln r_{pq}}{\partial n_q}) dl_q \tag{29}$$

where $A(p)$ is the solid angle at point p on the boundary and r_{pq} is the distance from the field point p to the source point q. Straight line elements, with variables varying linearly within each element, are distributed along the boundary. To perform integration over each element with nodes 1 and 2 in Eq. (29), we define

$$\mathbf{r} = x\mathbf{i} + y\mathbf{j} = \sum_{i=1}^{2} h^i(u) \cdot \mathbf{r}^i \ , \ \ \phi = \sum_{i=1}^{2} h^i(u) \cdot \phi^i \tag{30}$$

in which $\mathbf{r}$ is the position vector from the origin O with $\mathbf{i}$ and $\mathbf{j}$ being the unit vectors in the x and y directions, respectively. The shape functions are chosen as

$$h^1(u) = 1 - u \ , \ \ h^2(u) = u \tag{31}$$

where $0 \le u \le 1$. Substituting Eqs. (30) and (31) into Eq. (29), we have

$$A(p)\varphi(p) = \sum_{j=1}^{N_e} \int_0^1 \ln r_{pq} \sum_{i=1}^{2} h^i(u) \frac{\partial \varphi_j^i(q)}{\partial n} l_j du - \sum_{j=1}^{N_e} \int_0^1 \frac{\partial \ln r_{pq}}{\partial \mathrm{n}} \sum_{i=1}^{2} h^i(u) \varphi_j^i(q) l_j du \tag{32}$$

where N_e is total number of elements, and l_j is the length or Jacobian of each element. The integrations within each element can be obtained explicitly as in Lu et al. (2000).

2.4. The pressure

The pressure in the flow field can be obtained through the Bernoulli equation

$$P - P_0 = -\phi_t - \frac{1}{2}|\nabla \phi|^2 + \frac{1}{2}u_0^2 - (y - \Delta h) \tag{33}$$

The velocity potential ϕ can be solved at each time step through the numerical scheme in the previous section, from which its gradient $\nabla \phi$ can be obtained. However the temporal derivative of potential ϕ_t is still unknown explicitly. To deal with this problem, the auxiliary function method is adopted (Wu and Eatcok Taylor, 1996, 2003). We notice that ϕ_t also satisfies the Laplace's

function in the fluid domain. The normal derivative of ϕ_t on the body surface can be written as (Wu, 1998)

$$\frac{\partial \phi_t}{\partial n} = \left(\dot{\mathbf{U}} + \dot{\mathbf{\Omega}} \times \mathbf{X}\right) \cdot \mathbf{n} - \mathbf{U} \cdot \frac{\partial \nabla \phi}{\partial n} + \mathbf{\Omega} \cdot \frac{\partial}{\partial n}\left[\boldsymbol{X} \times \left(\mathbf{U} - \nabla \phi\right)\right] \tag{34}$$

where $\mathbf{U} = U\mathbf{i} + V\mathbf{j}$, $\mathbf{\Omega} = \Omega\mathbf{k}$ with $\mathbf{k} = \mathbf{i} \times \mathbf{j}$, and the dot means the temporal derivative. A particular attention should be paid to the accelerations in Eq. (34), which are unknown before the force is found. To uncouple their nonlinear mutual dependence, we define

$$\phi_t = \chi_0 + \dot{U}\chi_1 + \dot{V}\chi_2 + \dot{\Omega}\chi_3 \tag{35}$$

Here $\chi_i (i = 0, \cdots 3)$ satisfy the Laplace's equation. The body surface boundary conditions for the auxiliary functions can respectively be written as

$$\begin{aligned} \frac{\partial \chi_0}{\partial n} &= -\mathbf{U} \cdot \frac{\partial \nabla \phi}{\partial n} + \mathbf{\Omega} \cdot \frac{\partial}{\partial n}\left[\boldsymbol{X} \times \left(\mathbf{U} - \nabla \phi\right)\right] \\ &= -(W + \Omega X)\frac{\partial \phi_y}{\partial n} + (-U + \Omega Y)\frac{\partial \phi_x}{\partial n} + \Omega[n_x(W - \phi_y) - n_y(U - \phi_x)] \end{aligned} \tag{36}$$

$$\frac{\partial \chi_1}{\partial n} = n_x \tag{37}$$

$$\frac{\partial \chi_2}{\partial n} = n_y \tag{38}$$

$$\frac{\partial \chi_3}{\partial n} = (Xn_y - Yn_x) \tag{39}$$

On the bottom, we have

$$\frac{\partial \chi_i}{\partial n} = 0, (i = 0,1,2,3) \tag{40}$$

On both the inner and outer free surfaces, the auxiliary functions related to the accelerations are assumed to be zero

$$\chi_i (i = 1,2,3) = 0 \tag{41}$$

while

$$\chi_0 = -\frac{1}{2}\left|\nabla \phi\right|^2 + \frac{1}{2}u_0^2 - (y - \Delta h) - P_0\left[\left(\frac{V_0}{V}\right)^{\gamma} - 1\right] \tag{42}$$

on the inner free surface and

$$\chi_0 = -\frac{1}{2}\left|\nabla \phi\right|^2 + \frac{1}{2}u_0^2 - (y - \Delta h) \tag{43}$$

on the outer free surface. At the far field, the boundary conditions take the form

$$\frac{\partial \chi_i}{\partial n} = 0, (i = 0,1,2,3), x \to \infty \tag{44}$$

The second derivatives in Eq. (34) may cause numerical difficulty. We adopt the method in Xu and Wu (2013) and use the following relationship

$$\frac{\partial \phi_y}{\partial n} = \frac{\partial \phi_x}{\partial l}, \quad \frac{\partial \phi_x}{\partial n} = -\frac{\partial \phi_y}{\partial l} \tag{45}$$

where $\mathbf{l}$ is along the tangential direction of body surface and is obtained by rotating $\mathbf{n}$ by 90 degrees anti-clockwise, and thus $l_x = -n_y$ and $l_y = n_x$. In the stretched system, we define

$$\phi_t = \chi_0' + \dot{U}s\chi_1' + \dot{V}s\chi_2' + \dot{\Omega}s\chi_3' \tag{46}$$

Similar to Eqs. (36-39), the body surface boundary conditions for the auxiliary functions in the stretched system can respectively be written as

$$\begin{aligned}\frac{\partial \chi_0'}{\partial n} &= -\mathbf{U}\cdot\frac{\partial \nabla\phi}{\partial n} + \mathbf{\Omega}\cdot\frac{\partial}{\partial n}\left[\boldsymbol{X}\times\left(\mathbf{U}-\nabla\phi\right)\right] \\ &= -(W+\Omega X)\frac{\partial(\varphi_\alpha \sin\gamma + \varphi_\beta\cos\gamma)}{\partial n} + (-U+\Omega Y)\frac{\partial(\varphi_\alpha\cos\gamma - \varphi_\beta\sin\gamma)}{\partial n} \\ &\quad + s\Omega[(n_\alpha\cos\gamma - n_\beta\sin\gamma)(W-\varphi_\alpha\sin\gamma-\varphi_\beta\cos\gamma) \\ &\quad -(n_\alpha\sin\gamma + n_\beta\cos\gamma)(U-\varphi_\alpha\cos\gamma+\varphi_\beta\sin\gamma)]\end{aligned} \tag{47}$$

$$\frac{\partial \chi_1'}{\partial n} = n_\alpha\cos\gamma - n_\beta\sin\gamma \tag{48}$$

$$\frac{\partial \chi_2'}{\partial n} = n_\alpha\sin\gamma + n_\beta\cos\gamma \tag{49}$$

$$\frac{\partial \chi_3'}{\partial n} = [X(n_\alpha\sin\gamma + n_\beta\cos\gamma) - Y(n_\alpha\cos\gamma - n_\beta\sin\gamma)] \tag{50}$$

In these equations and those below, the following relationship is to be adopted

$$X = (s\alpha + \xi_{\mathrm{p}})\cos\gamma - (s\beta + \eta_{\mathrm{p}})\sin\gamma \tag{51}$$

$$Y = (s\alpha + \xi_{\mathrm{p}})\sin\gamma + (s\beta + \eta_{\mathrm{p}})\cos\gamma \tag{52}$$

The boundary conditions for the auxiliary functions on the inner and outer free surfaces retain the same form as that in Eqs. (42-43). At the far field, the boundary conditions can be written as

$$\frac{\partial \chi_0'}{\partial n} = \frac{\partial \phi_{It}}{\partial n}, \alpha = L \tag{53}$$

$$\frac{\partial \chi_i'}{\partial n} = 0, (i = 1,2,3), \alpha = L \tag{54}$$

The values on the right hand side of Eq. (53) are estimated through the linear interpolation based on the values on the upper and lower free surfaces (Song, 2015). When the dual stretched and normal physical systems are involved in the calculation, the auxiliary function method can still be used. They will be solved in the two separate domains and continuity conditions will be enforced on their interface. The procedure is virtually identical to that for the potential itself, described previously. After the initial stage, when the wetted body surface is no longer a small fraction of the characteristic length, for example the body dimension, the stretched coordinate system will be no longer needed and computation can be conducted in the single physical domain.

2.5. The body motion

Based on Newton's law, the motion of body can be written as

$$[\mathbf{M}][\mathbf{A}] = [\mathbf{F}] + [\mathbf{F}_e] \tag{55}$$

where

$$\mathbf{M} = \begin{bmatrix} m & 0 & 0 \\ 0 & m & 0 \\ 0 & 0 & I \end{bmatrix}, \ [\mathbf{A}] = \begin{bmatrix} \dot{U} \\ \dot{V} \\ \dot{\Omega} \end{bmatrix}, \ \mathbf{F} = \begin{bmatrix} F_1 \\ F_2 \\ F_3 \end{bmatrix}, \ \mathbf{F}_e = \begin{bmatrix} 0 \\ -m \\ 0 \end{bmatrix}$$

In the above equation, m is the mass of the two dimensional floating body, with the moment of inertia, I, with respect to the centre of mass. The hydrodynamic force in Eq. (55) can be obtained through the integration of pressure $P - P_0$ in Eq. (33) along the body surface in contact with bubble and water including the impact area. Based on the definition of auxiliary functions in Eq. (35), we note that the terms of unknown accelerations appear on the right hand side of Eq. (55). These unknown terms can be moved to the left hand side of Eq. (55), and the following coupled equation of motion is established as a result

$$[\mathbf{M} + \mathbf{C}][\mathbf{A}] = [\mathbf{Q}] + [\mathbf{F}_e] \tag{56}$$

where $[\mathbf{C}]$ is a matrix with the coefficients

$$C_{ij} = \int_{S_0} \chi_i n_j dS \tag{57}$$

and matrix $[\mathbf{Q}]$ can be obtained through

$$Q_i = -\int_{S_0} [\chi_0 + \frac{1}{2}|\nabla\phi|^2 - \frac{1}{2}u_0^2 + (y - \nabla h)] \cdot n_i dS \tag{58}$$

where S_0 covers bubble surface and wetted surface. The latter includes the impact area S_I on which the integration is performed in the stretched system at the initial stage. We have the contribution from this part as

$$C_{ij} = s^2 \int_{S_I} \chi_i n_j dS \tag{59}$$

$$Q_i = -s\int_{S_I} \{\chi_0 + \frac{1}{2}|\nabla\varphi|^2 - \frac{1}{2}u_0^2 + [y_G + (s\alpha + \xi_p)\sin\gamma + (s\beta + \eta_p)\cos\gamma - \nabla h]\} \cdot n_i dS \tag{60}$$

where $i, j = 1, 2, 3$.

3. Numerical results and discussions

The initial parameters for the overturning wave are set as $u_0 = 1.1623$ and $x_0 = 10$ respectively, and correspondingly $\Delta h = 1.5$. The still water depth is set as 1.0 in non-dimensional sense, and ν is set as 0.5. These are the same as those in Cooker and Peregrine (1990). Correspondingly, the non-dimensional atmospheric pressure is 10.087. The width and initial draught of a rectangular floating body used in the study are set as 0.3 and 0.515 respectively, and the corners on the two sides of bottom are replaced by a quarter circle with a radius of 0.015. The initial position of the centre of gravity of the body is set as $(x_G, y_G) = (0, -0.25)$, the mass as 0.156, which is

the same as the fluid force in vertical direction at $t = 0$, and the rotational inertia is set as 0.1. The floating body may be used as typical representations for various ocean engineering problems. For example, it can be used to represent overturning wave impact on a two dimensional cross section of a floating ship. In such a case, a moving ship may not have additional restoring force apart from the hydrostatic ones. Therefore its cross section has the full three degrees of freedom. Even when a ship is anchored, the cable anchorage may provide some additional restoring force, but it does not completely restrain the motions. Another example which can be represented by the present configuration is that the overturning wave impact on floating breakwaters which commonly have two types based on the way in which the body is anchored to seabed. The first type is the vertical pile-restrained floating breakwater, in which the body is allowed to have vertical response, or heave, while horizontal and rotational motions, or surge and roll, are restrained. The second type is the tethered floating breakwater, in which the floating body is anchored to seabed through a group of mooring cables, and all three degrees of motions in two-dimensional sense are allowed. The third example is the tension leg platform (TLP), in which the floating body is connected to seabed through tendons, which may be treated as massless springs. In such a case, the additional restoring forces to the body motion are all related to the variation of the length of tendons and they are not independent. A further example which may be presented by the present configuration is when the body is completely restrained or fixed. If its draught extends to seabed or is sufficiently deep, it represents the case of a coastal wall. In following simulations, the selected cases reflect the examples above, and the last case is mainly used for convergence study.

3.1. Convergence study and comparison

In order to verify the reliability and accuracy of the methodology and numerical procedure in the paper, we first consider the case of an overturning wave impacting a fixed body which resembles a coastal wall, especially if the draught is large. The width of the rectangular computational domain is set as $|x| = 16$ in the physical system and $L = 4$ in the stretched system. In stage 1, in which the wave front has not touched the body, the body surface and the free surface below the wave front which will become the bubble surface after the impact are both discretised with elements of size l_m. At the wave front, where the free surface has the largest curvature, the element size is set as $0.5l_m$. Away from this area, the size of element increases gradually at a fixed ratio δ, and the largest element size is not allowed to be bigger than 0.5, while in the cases below it actually has not exceeded 0.32. In stage 2, when the wave front hits the body surface and the dual stretched and physical coordinate systems are used in the calculation, the element distribution in the physical system is the same as that in stage 1. In the stretched system, the elements of equal size l_n are distributed along the impact area, and the sizes of elements on both the outer and inner free surface increase gradually at the ratio δ from the body. The size of the element near the interface with the physical domain is the same as that in stage 1. In stage 3, which starts when the stretching ratio $s \approx 0.07$, the computation is conducted in a single physical domain. The element sizes on the body surface below the air bubble are set as l_n, while those on the body surface above the air bubble are

set as $0.5l_n$ .On the inner free surface, the element side increases gradually from the impact zone to the main body zone at the fixed ratio δ , and the largest one is no bigger than l_n . The element size on the outer free surface increases gradually at the fixed ratio δ , and the largest element size is no bigger than 0.5. In the following simulations, the thin jet is regularly cut once the jet thickness is smaller than $0.01l_n$, or when the two tips inside the bubble meet.

Assume that the overturning wave hits the body at $t = t_0$. Strictly speaking, the impact starts when the tip of the wave front touches the body surface. However, we start the simulation at a tiny wetted contact surface or an initial stretching ratio $s_0 = 8.7 \times 10^{-4}$, which corresponds to $t_0 = 5.26608$ in the present case. Figs. 4 (a) and (b) give the pressure distributions at $s / s_0 = 10$ and $s / s_0 = 20$ respectively, in which the horizontal coordinate y' is parallel to the symmetry axis of body and measured from the bottom. The ratio δ for element size increase is set as 1.02. Based on the discussion in Sun and Wu (2013), and Sun et al. (2015), at the initial moment of water entry, the boundary conditions on the liquid surface at $s = s_0$ are assumed to be the same as those before the body touches the water. Thus the solution at this very early stage may not entirely correspond to the true physics, as the boundary condition does not contain the disturbance. However, when s_0 is sufficiently small, after a period of numerical transition, the initial results do not have significant effect on those at later stage. For this reason, it can be seen from Figs. 4(a) and (b) that, when $s / s_0 = 10$ and 20, there is hardly any visible difference between the two curves from the two different meshes. In fact the average relative errors between them are 0.98% in Figs. 4(a) and 1.62% in Figs. 4(b). This suggests that a mesh independent result has been achieved. Based on this, we may also disregard the results between $s / s_0 = 1$ and 10 and assume that the results from the simulation are meaningful only when $s / s_0 \geq 10$. This will not cause any real problem for practical applications as s_0 can be as small as desired based on the requirement of accuracy. The time histories of horizontal force F_1 , vertical force F_2 and rotational moment F_3 including both the dynamic wave exciting and hydrostatic force, and history of air bubble volume V at different meshes are given in Figs. 4(c~ f) respectively, from $s \approx 10 s_0$ ($t - t_0 \approx 4.7 \times 10^{-4}$). It can be seen that the results from different meshes are virtually graphically identical. The average relative errors are only 0.44%, 0.12%, 0.47% and 0.06% respectively. This also indicates that the present numerical procedure is mesh independent.

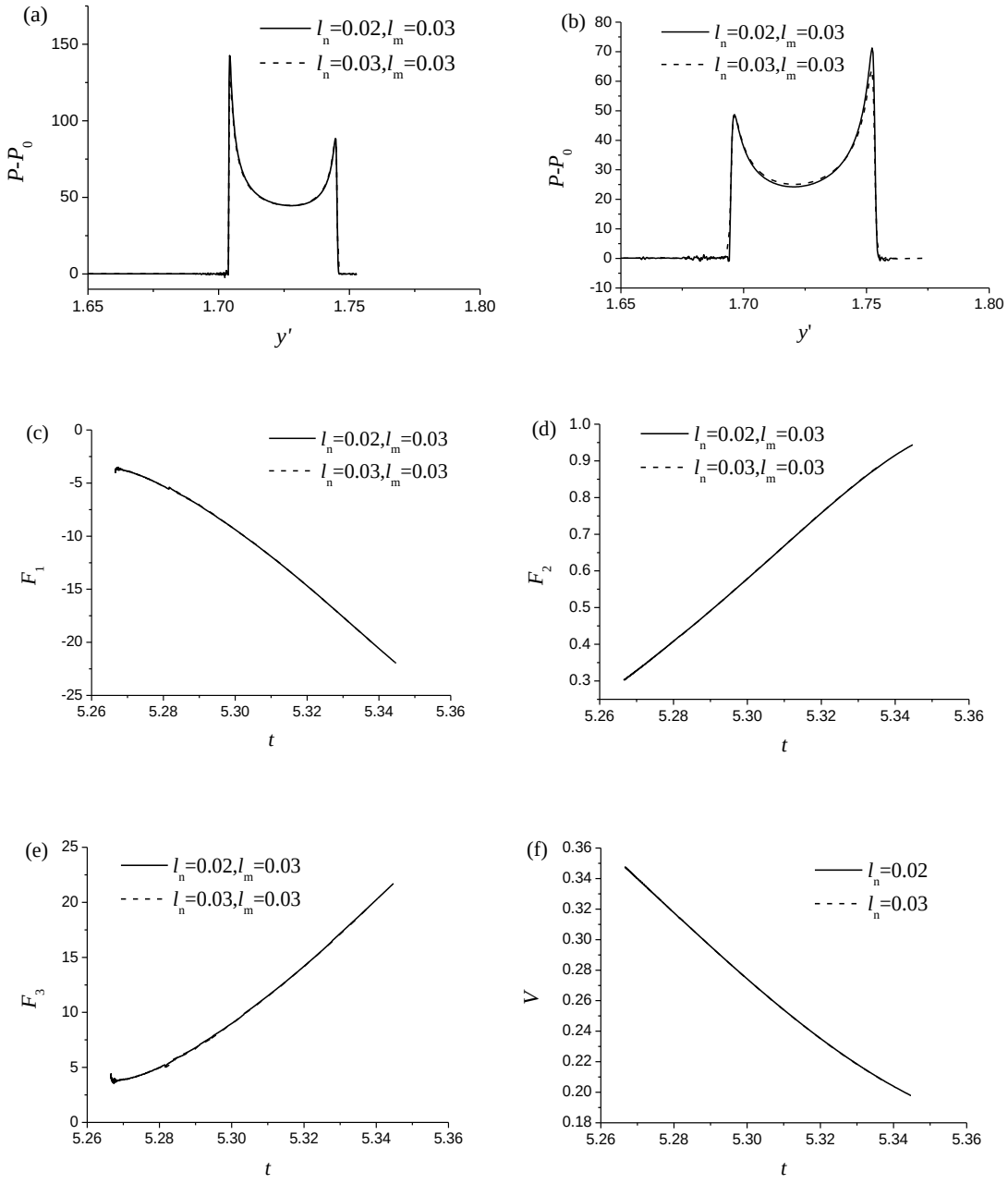

Fig.4. Mesh convergence study (a) the pressure distribution at $s/s_0 = 10$, (b) the pressure distribution at $s/s_0 = 20$, and the time histories of (c) F_1, (d) F_2, (e) F_3 and (f) air bubble volume V.

In stage 1, as the wave is propagating and an overturning wave will be formed, the time step dt, is taken from the ratio of $l_m / (\mu_0 V_{\max})$, where $V_{\max}$ is the maximum of the velocity magnitude on the free surface at each time step. μ_0 is a coefficient, and taken as 5 in this stage. Just before the wave front touches the body, or when the distance between the tip of wave front and body is smaller than $0.2l_m$, a small time step $dt = 2.5\times10^{-5}$ is used. This is to avoid the situation in

which $s=0$ at t and then relatively large $s=s_0$ at $t+dt$. In stage 2, the time step is set through $ds=s_0/n$ based on the requirement of the stretched system. This gives a time step $dt=ds/s'(t)$. In stage 3, the time step is switched back to $dt=l_n/(\mu V_{\max})$. The comparison of results from two different time steps are presented in Fig. 5 to verify convergence. In the first case, the time step increases gradually in stage 2, and this can be realized by setting $n=100$ in the first 200 steps, then $n=50$ from steps 200 to 400, and $n=10$ from 400th time step. μ in the stage 3 is set as 10. In the second case, the corresponding time steps are doubled. This means that the corresponding n and μ in the previous case are reduced by half. It is evident that the pressures in Figs. 5(a) and (b) from two different time steps are almost coincident. The relative errors are 1.24% and 2.65% respectively. The curves for the time histories of forces and the curves for cavity volume in Figs. 5(c~f) respectively are graphically identical. The average relative errors are only 0.34%, 0.08%, 0.32% and 0.07% respectively. These results indicate that the present numerical procedure is time step independent. In the following simulations, unless it is specified, mesh is based on $l_m=0.03$, $l_n=0.03$, $\delta=1.02$, time step is set based on those parameters in case one of Fig.5 and μ_0=5.

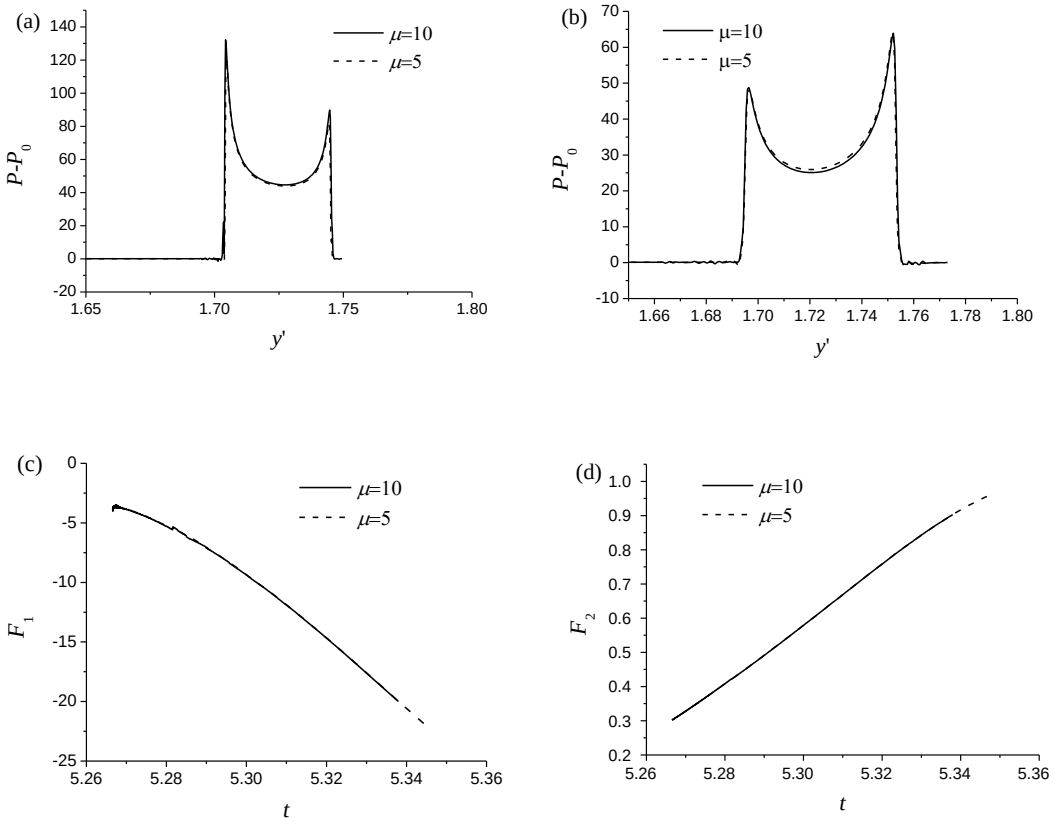

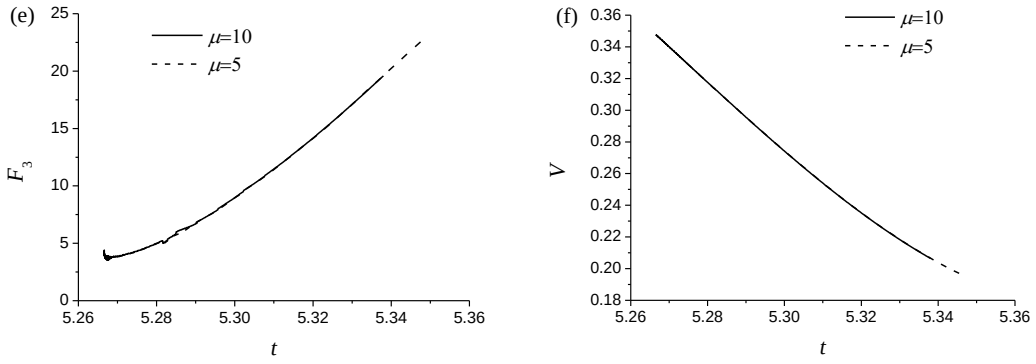

Fig. 5. Convergence study with time step (a) the pressure distribution at $s/s_0 = 10$, (b) the pressure distribution at $s/s_0 = 20$, and the time histories of (c) F_1, (d) F_2, (e) F_3 and (f) air bubble volume V.

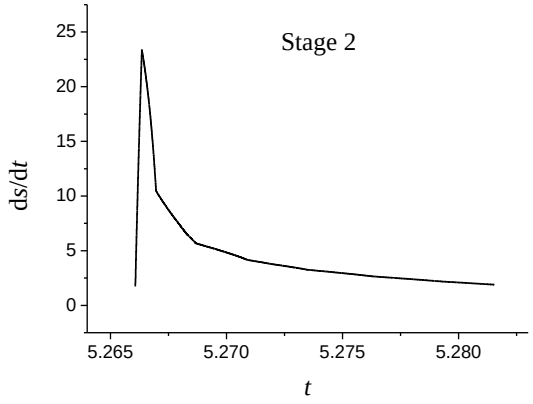

Fig. 6. The time history of the temporal derivative of impact area ds/dt.

Based on the result from the simulation, it has been observed that impact occurs at $t = t_0 \approx 5.26608$. The force on the body rises rapidly or virtually vertically to a peak and then it drops to a value which is the starting point of the force history at $t = t_2 \approx t_0 + 4.7\times10^{-4}$ in Figs. 4 and 5. This nearly vertical rise may contradict to Eq. (60) which implies that the force should vary with s continuously and starts from 0 when $s = 0$. However as can be seen from Fig. 6, ds/dt increases very rapidly due to the fact that the wave front is quite blunt. This leads to a nearly vertical variation of force, especially F_1 and F_3, with respect to t. Within this very short period of time $t_2 - t_0$, the impact may be lumped together and the loading on the body can be measured through the impulse (Wu, 2001).

$$\Pi_i = \int_{t_0}^{t_2} F_i dt \tag{61}$$

Such an impulse model has in fact been used by Cooker (1996). The momentum change of a floating body from $t = t_0$ to $t = t_2$ can be obtained by Π_i. For example, for the horizontal one, $\Pi_1 = mu_{t_2} - mu_{t_0}$. Here $t_2 - t_0 = 4.7\times10^{-4}$, and Π_1 is roughly equal to 1.8×10^{-3}. This gives an estimated velocity variation of $\Delta u = u_{t_2} - u_{t_0} = 5.7\times10^{-3}$. Such a small variation due to the initial impulse is ignored in the subsequent calculations. After the impulse period, the wetted surface due to the wave front is no longer small, and the loading from this wetted surface is no longer negligible. Thus the force at $t = t_2$ ($s = s_2$) is not the same as that at $t = t_0$ ($s = s_0$). Beyond this point which approximately corresponds to $s_2 \approx 10 s_0$, the force begins to vary smoothly.

Fig. 7 gives the comparison between the results obtained from the present procedure and those from Cooker and Peregrine (1990) for a vertical wall. In such a case, the draught of the body in our case is taken the same as the water depth and then its motion will be completely restrained. The parameters of wave are kept the same as those in the previous cases apart from x_0 which is now set as 7.5, and they are the same as those in Cooker and Peregrine (1990). It can be seen from the figure that the present results for both free shape and pressure are in good agreement with those from Cooker and Peregrine (1990).

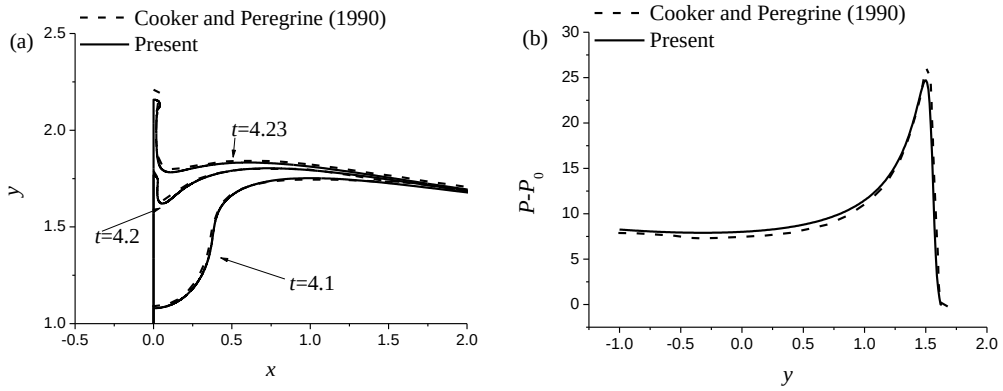

Fig. 7. Comparison of results for wave hitting a fixed vertical wall (a) the free surface and (b) the pressure distribution on the wall at $t = 4.19$.

3.2. Case studies

3.2.1 A floating body without external constraint

We first consider overturning wave impact on a body freely floating on the free surface. This reflects a cross section of a ship in beam sea. When the middle section of a slender ship does not change very much along the length, strip theory can be used to predict its motion. Here when the air bubble is trapped, strictly speaking its flow should be modelled by the two dimensional compressible flow theory for each section. However we adopt the simplified model based on the adiabatic model. This reflects a cross section of a ship in the sea. The parameters of incoming wave and body are the same as those used before, and the wave will hit the body at $t_0 = 5.26608$.

Although the body will respond to the wave and be sent into motion before impact occurs, we let it move only from $t \approx t_0 + 4.75\times10^{-4}$, which corresponds to $s \approx 10s_0$. During this short interval, the impulse stage discussed above has passed, and the small variation of velocity due to the impulse is neglected. Fig. 8 gives the free surface profile and pressure distribution on the front side of body at different $t - t_0$. As can be seen in Fig. 8(a), at the early stage of impact, represented by $t - t_0 = 0.001$, the area of the wetted surface at the impact zone is very small. Due to the large relative velocity between the wave front and body, a large impact pressure in Fig. 8(b) is generated on the wetted area. Within this impact zone, two peaks of the pressure can be observed, located at upper and lower jet roots respectively. It is evident that the former peak is larger than the latter one. This is due to the fact that the angle which is formed between the upper side of the body and free surface is smaller than that at the lower side, while the velocity magnitudes at the two places are found to be similar. A smaller deadrise angle usually corresponds to a larger impact pressure, as discussed by Sun et al. (2015). As t increases, the relative velocity between the body and wave front decreases, due to the fact that the overturning wave is being blocked as well as that the body has been set into motion, and this leads to the rapid decrease of impact pressure. Thus the impact pressure at $t - t_0 = 0.02$ is much smaller than that at 0.001, and a much smaller peak can be observed. Beyond that the pressure on the front side is more or less uniform. Its value is very close to that inside the trapped bubble and therefore oscillates in time with its volume.

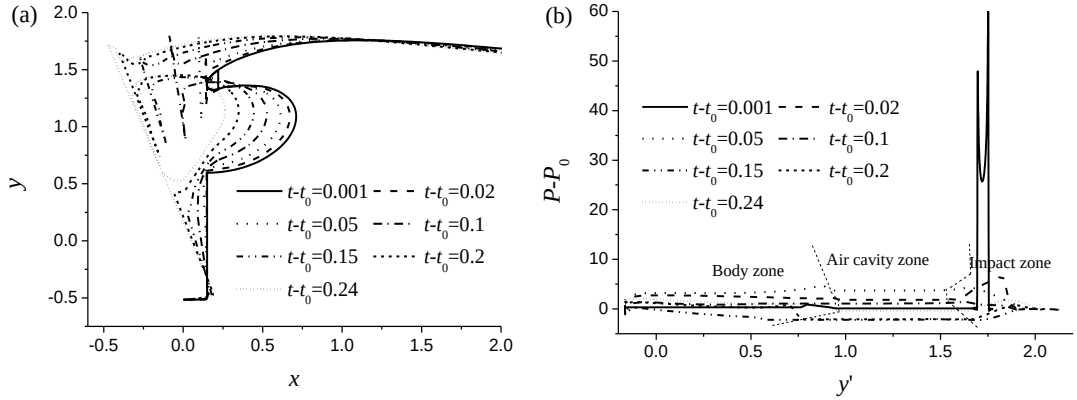

Fig. 8. (a) The free surface profile and (b) pressure distribution of an overturning wave impacting on a floating body at different time.

Fig. 9 presents the time histories of acceleration, velocity and displacement in three degrees of freedom, respectively, together with air bubble volume and air bubble pressure. When $t - t_0 < 0.02$, the wetted surface may be small however the impact pressure is relatively large, as can be seen from Fig. 8(b). This means that the overall fluid loading may be still significant. More importantly, as the impact point is significantly higher than the mean free surface, it leads to a large rotational acceleration, as can be seen in Fig. 9(c). After that, as the air bubble volume decreases, its internal pressure increases, and it gradually becomes the most important component in the resultant force. As can be observed from the pressure curve in Fig. 9(k), it reaches a peak at $t - t_0 \approx 0.07$.

As the pressure in the air bubble increases, the magnitudes of the accelerations in heave and roll also increase between $t-t_0 \approx 0.02$ and 0.07, as can be observed in Figs. 9(a) and (c). As time increases, the increased air bubble pressure will push the wave back and its volume will bounce back or increase. This will be helped by the motion of body which is being pushed away from the overturning wave. The pressure in the bubble will then decrease. As the air bubble expands, the pressure in the bubble may fall below the atmospheric pressure, which generates a suction force. This phenomenon can be observed between $t-t_0 \approx 0.12$ and 0.25 in Fig. 9(k). This will lead to the decrease of resultant force in $-x$ direction, and thus the horizontal acceleration in x direction increases in Fig. 9(a). This also leads to the decrease of rotational force, and the rotational acceleration in anticlockwise direction in Fig. 9(c) therefore decreases. Such a tendency will continue until the horizontal velocity in Fig. 9(d) is almost zero at $t-t_0 \approx 0.2$, near which the rotational velocity in Fig. 9(f) is also close to zero. After that, the air cavity begins to contract, and the air cavity pressure, resultant force, and the velocities of movement in Figs. 9(d) and (f) will then increase again.

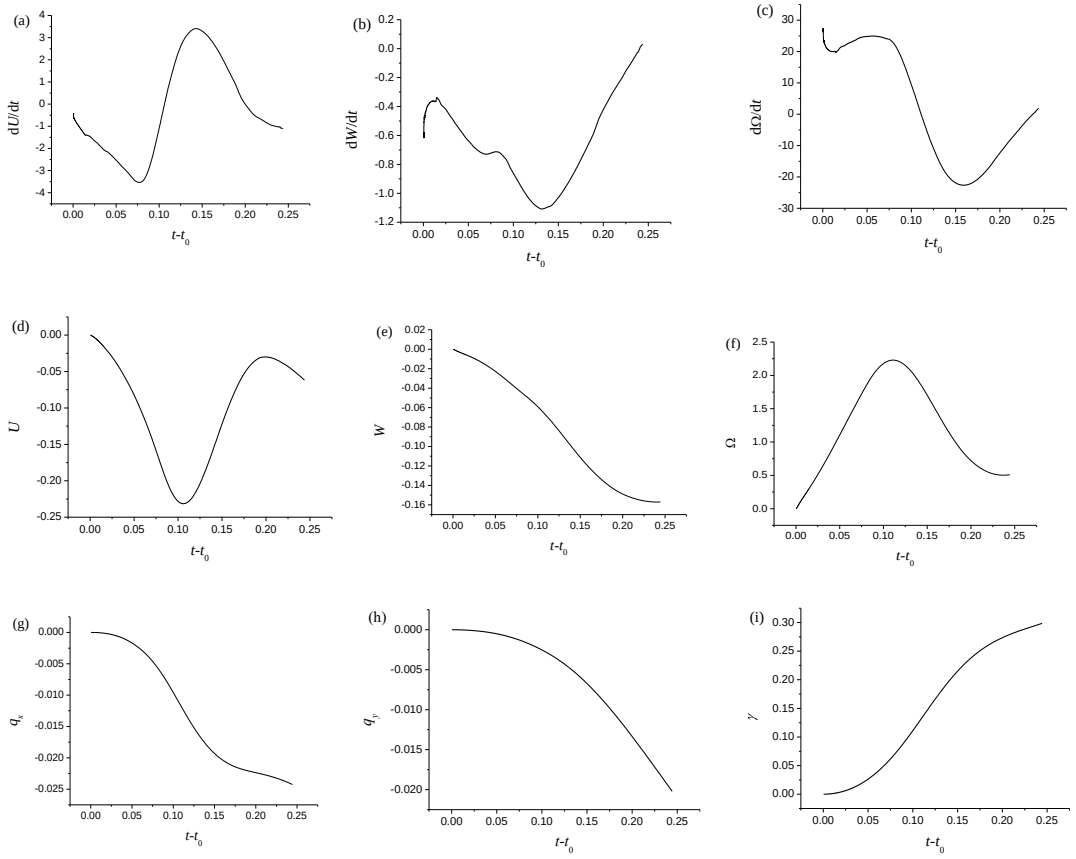

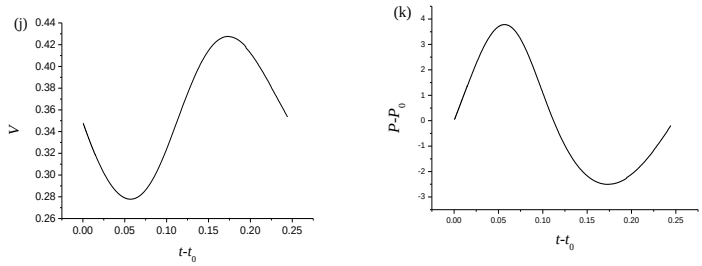

Fig.9. The time histories of (a)horizontal acceleration, (b)vertical acceleration, (c)rotational acceleration, (d)horizontal velocity, (e)vertical velocity, (f)rotational velocity, (g)horizontal displacement, (h)vertical displacement, (i)rotational displacement, (j)air bubble volume and (k)air bubble pressure.

3.2.2 A floating body tethered to seabed through mooring cables

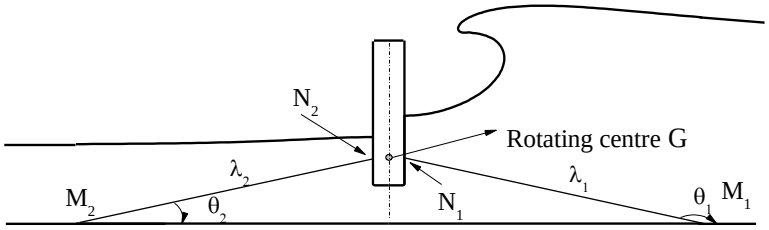

Fig. 10. Floating breakwater with a cable system.

The floating breakwaters are usually placed at a location where the wave motion is largest, and it is often tethered to seabed through a group of mooring cables, and the buoyancies and weights of cables are both neglected. Typically, the floating breakwaters are long, and the section of structure does not change very much for a buoyant box or raft. The two-dimensional theory is used here for the similar reasons discussed in section 3.2.1. Fig. 10 gives a typical case of a floating breakwater anchored to seabed, and the motion of body is restrained by two cables. In mathematical modelling, the cable is usually treated as a massless spring, and only the effect of axial stiffness is considered. The angles between x axis and the cables on the right and left sides are denoted as θ_1 and θ_2 respectively, while their lengths are λ_1 and λ_2 respectively, which will both vary with the motion of body. At $t = 0$, they are correspondingly denoted as θ_{01}, θ_{02}, λ_{01} and λ_{02}. The ends of the two cables fixed on body are denoted as N_1 and N_2 respectively, while those fixed on the seabed are denoted as M_1 and M_2 respectively. (ξ_i, η_i) represent the coordinates of N_i in the body fixed system, while (x_{M_i}, y_{M_i}) denote the coordinates of $M_i, (i = 1,2)$ in the earth fixed system. The displacements of ends fixed on body can be expressed as

$$\Delta x_i = q_x + \xi_i(\cos\gamma - 1) - \eta_i \sin\gamma \tag{62}$$

$$\Delta y_i = q_y + \xi_i \sin\gamma + \eta_i(\cos\gamma - 1) \tag{63}$$

where q_x and q_y are defined in Eqs. (17) and (18). The variation of λ_i due to body motion can be given as

$$\Delta\lambda_i = \sqrt{(\lambda_{0i}\cos\theta_{0i} + \Delta x_i)^2 + (\lambda_{0i}\sin\theta_{0i} + \Delta y_i)^2} - \lambda_{0i} \tag{64}$$

in which

$$\theta_i = a\cos[(\lambda_{0i}\cos\theta_{0i} + \Delta x_i)/(\lambda_{0i} + \Delta\lambda_i)] \tag{65}$$

The force along the cable is calculated based on Hooke's law

$$T_i = k\Delta\lambda_i + T_{0i} \tag{66}$$

where k is the stiffness coefficient of the cable and T_{0i} is its pre-tension force which satisfies $T_{01}\sin\theta_{01} + T_{02}\sin\theta_{02} + m = F_B$ and $T_{01}\cos\theta_{01} + T_{02}\cos\theta_{02} = 0$ to guarantee the balance of force on the body in calm water, where F_{B} is the buoyancy. T_i from each cable will lead to forces and moment on the body and will be incorporated into the equation (56) through

$$F_e = \begin{bmatrix} -T_1\cos\theta_1 - T_2\cos\theta_2 \\ -T_1\sin\theta_1 - T_2\sin\theta_2 - m \\ -T_1\sin(\theta_1-\gamma)\cdot\xi_1 - T_2\sin(\theta_2-\gamma)\cdot\xi_2 + T_1\cos(\theta_1-\gamma)\cdot\eta_1 + T_2\cos(\theta_2-\gamma)\cdot\eta_2 \end{bmatrix} \tag{67}$$

The parameters of the floating body considered here are the same as those presented at the beginning of section 3, apart from the mass which is now taken as 0.1. The two cables are symmetric about the centre line of body at $t = 0$, with $\theta_{02} = 8^\circ$ and $\theta_{01} = 172^\circ$. In such a case, we have the pre-tension force $T_{01} = T_{02} = 0.2$. The y coordinates of N_1 and N_2 are the same as that of the mass centre, or their coordinates in the body-fixed system are $(0.15, 0)$ and $(-0.15, 0)$ respectively, where 0.15 is the half width of the body. This corresponds to a vertical distance $\lambda_{01}\sin\theta_{01} = 0.75$, which is comparable to the draught of body 0.515. As both cables have a small slope, the horizontal motion of the body will be very much restrained. Fig. 11 provides the velocities and displacements in three degrees of freedom, respectively, together with the air bubble volume and pressure at different stiffness. When the stiffness k is zero, the cable has only the pre-tension force which is constant. Under the action of fluid force, air bubble force and the pre-tension force, the magnitude of the horizontal velocity in Fig. 11(a) increases first and then decreases, and the sign is negative throughout the whole simulation. The magnitude of the vertical velocity in Fig. 11(c) decreases and the sign remains negative. The floating body continually moves to the left and downwards, as shown in Figs. 11(b) and (d). The rotational velocity increases to a peak and then decreases. The motion in this case is similar to that in section 3.2.1. For non zero k, it is not possible for the body to continually move away from its mean position. It would be pulled or pushed back by the cables and begin to oscillate around the mean position. When k is larger, the body is

expected to pulled back earlier and therefore has a smaller motion amplitude and larger frequency. This is particularly evident in the horizontal mode for which the cable provides the main constraint. If we consider the case in which the body rotates about its fixed mass centre, λ_1 and λ_2 will increase or decrease together when γ is small. Therefore the moments created by the two cables will cancel each other when γ is small, for example before $t = 0.1$, during this period the cables have small effects on the roll motion. When γ is not small, λ_1 and λ_2 will be noticeably affected by the variation of γ. Thus When γ becomes larger, some difference of rotational motion from different stiffness k can be found. Since the restrained moment is small relative to the fluid rotational moment, the difference is not very prominent. This is also reflected by Figs. 11(e) and (f), which show the rotational velocity and displacement are not significantly affected by k at $t - t_0 < 0.1$. After that, some difference can be observed.

As k becomes very large, the results are expected to tend to those at $k \to \infty$. We should note that at $k \to \infty$, it is still possible for the body to have motion. This is because although λ_1 and λ_2 will no longer change, it provides only two constraints given in Eq. (64) while the body has three degrees of freedom. However it is expected in such a case that the sway, heave and roll motions should be linked to a single parameter as there is effectively only one degree of freedom. In fact, we can substitute Eqs. (62) and (63) into (64) and impose $\Delta\lambda_1 = \Delta\lambda_2 = 0$. q_x and q_y can then be written in terms of γ. The numerical results at large k in Figs. 11(b, d, f) are found to satisfy these two equations accurately. It is interesting to notice that the orders of γ, q_y and q_x are 10^{-1}, 10^{-2} and 10^{-3} respectively, as expected from this kind of restraint.

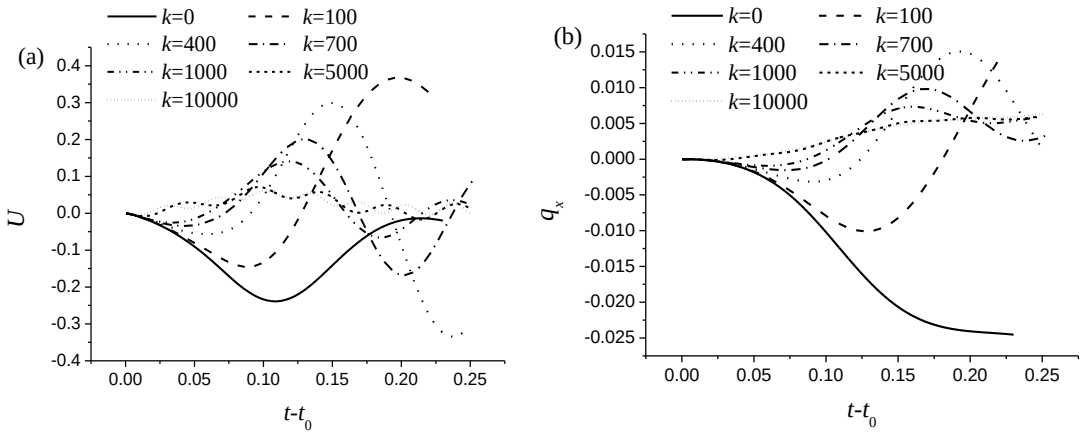

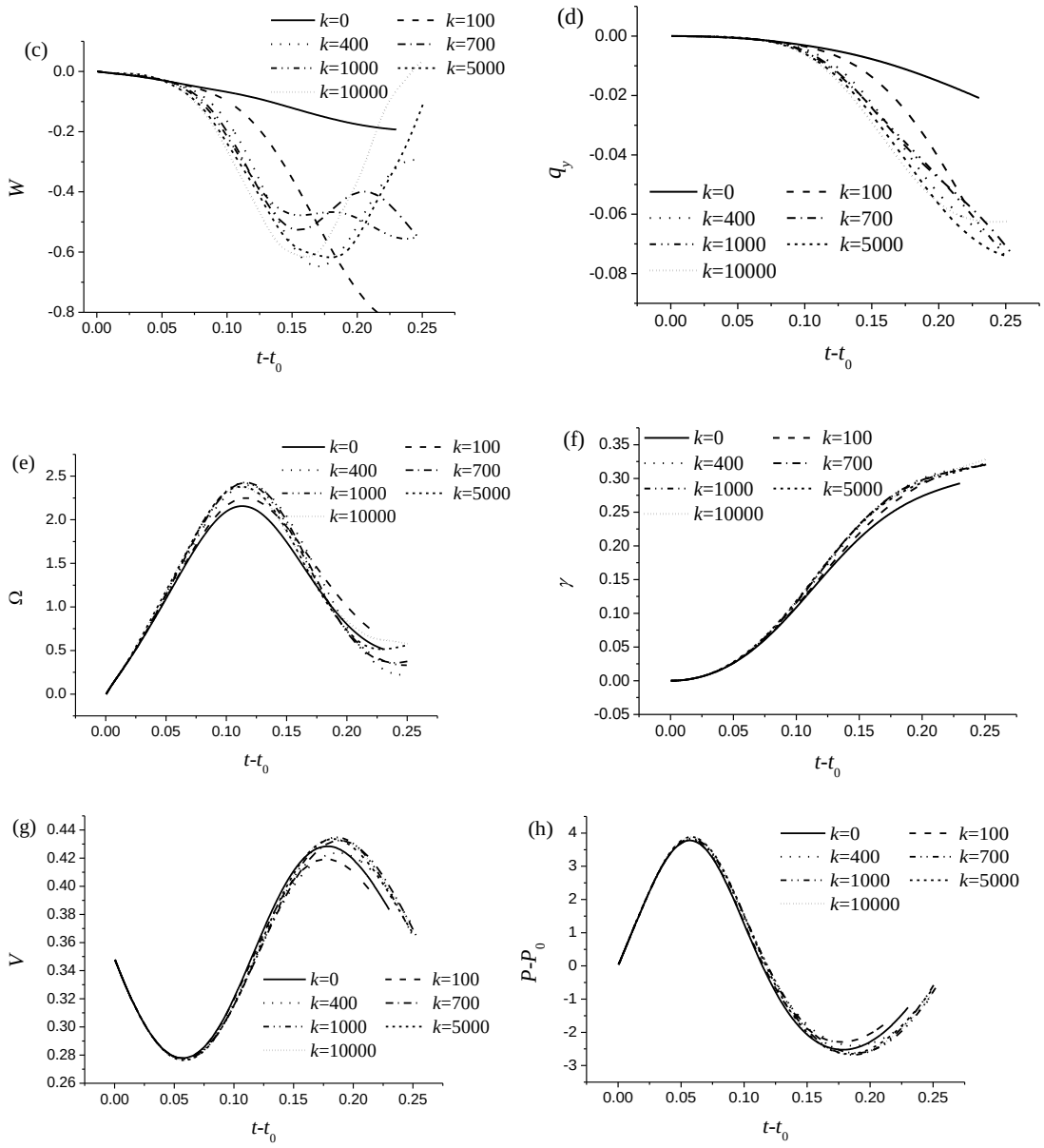

Fig. 11. The time histories of (a) horizontal velocity, (b) horizontal displacement, (c) vertical velocity, (d) vertical displacement, (e) rotational velocity, (f) rotational displacement, (g) the volume and (h) the pressure of air bubble for a floating breakwater at different cable stiffness.

3.2.3 A floating body constrained by tendons attached on bottom

In the following case, the two tendons will be placed vertically below a floating body, or $\theta_{01} = \theta_{02} = \pi / 2$. Such a form of restraint can often be found in tension leg platforms (TLP). A TLP is generally not a slender body and the 3D should be used for such a geometrical configuration. However the results from the present 2D simulations can still be expected to provide some overall insights into the problem. The tendon is treated as a spring with no mass, and only the effect of axial stiffness is considered. In this case, the width and draught of the floating body are both set as 0.5, the mass and rotating inertial are set as 0.1 and 2 respectively. The initial position of rotating centre is $(0,-0.25)$ in the space-fixed system. The ends of the tendons on the body in body-fixed system

are located at $(0.25,-0.25)$ and $(-0.25,-0.25)$ respectively. From the balance of force at $t=0$, we have $T_{01}=T_{02}=8.17\times10^{-2}$. Typically, the water depth at which a TLP operates is much larger than its draught. However, the breaking wave model given by Eq. (1) can still be used to represent some realistic cases. In such a case the initial length λ_0 is set as 30, which is much larger than the water depth in Eq. (1) to reflect a realistic ratio of tendon length to the TLP draught. The tendons will mainly provide the restraint in vertical direction while they provide far smaller restraints in other directions when their lengths are long. From Figs. 12(a) and (b), it can be seen that after impact, the body will be simply pushed away in the horizontal direction. The tendons offer very little resistance, even at very large k. The effect of tendons in the vertical direction is obvious in Figs. 12(c) and (d). As k increases, the motion becomes smaller. However as the stiffness becomes larger, the natural frequency of the body in heave becomes higher. The body motion after impact becomes highly oscillatory. This is consistent with a typical feature of a TLP, ie, ringing. As discussed by Zhou and Wu (2015), when a TLP is set into motion by a transient wave, it may have persistent oscillation at high frequency even long after the wave has passed the body. The effect of k on q_x becomes obvious at later stage of the impact, as shown in Fig. 12(b). Correspondingly, the effects of k on bubble volume and pressure are also evident at the later stage of impact, as shown in Figs. 12(g) and (h).

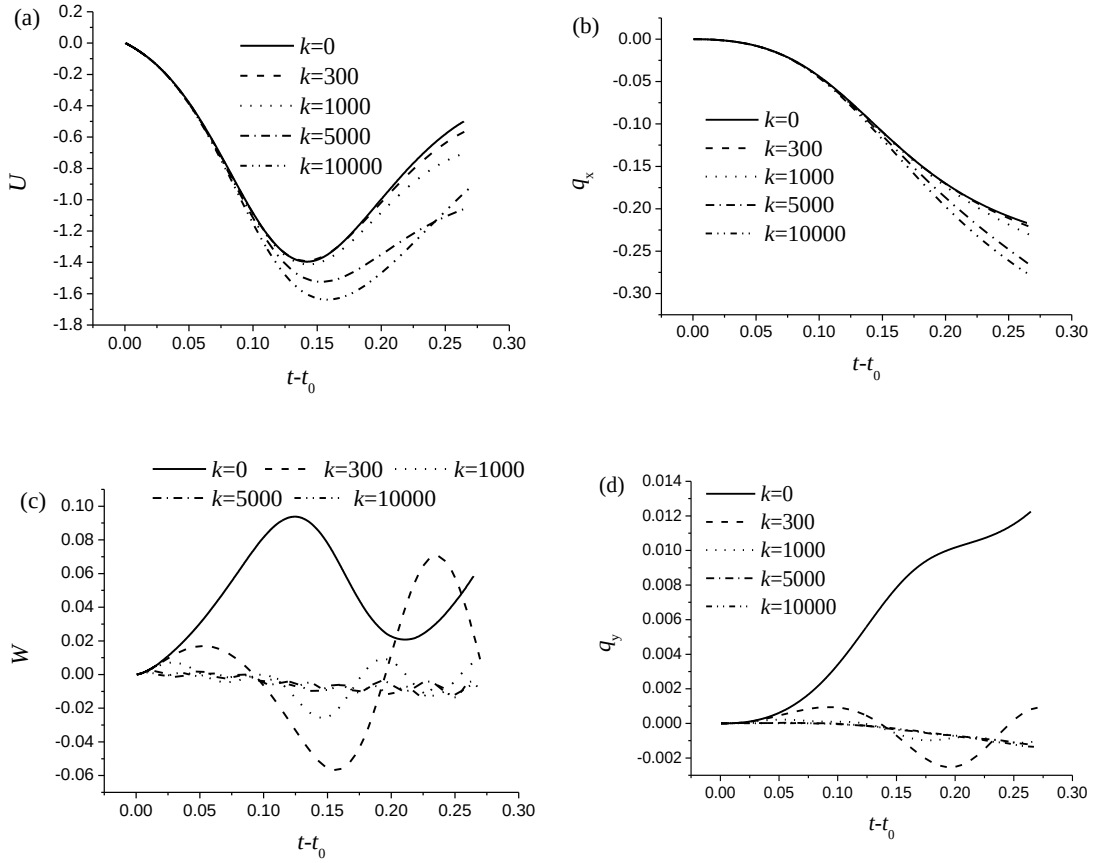

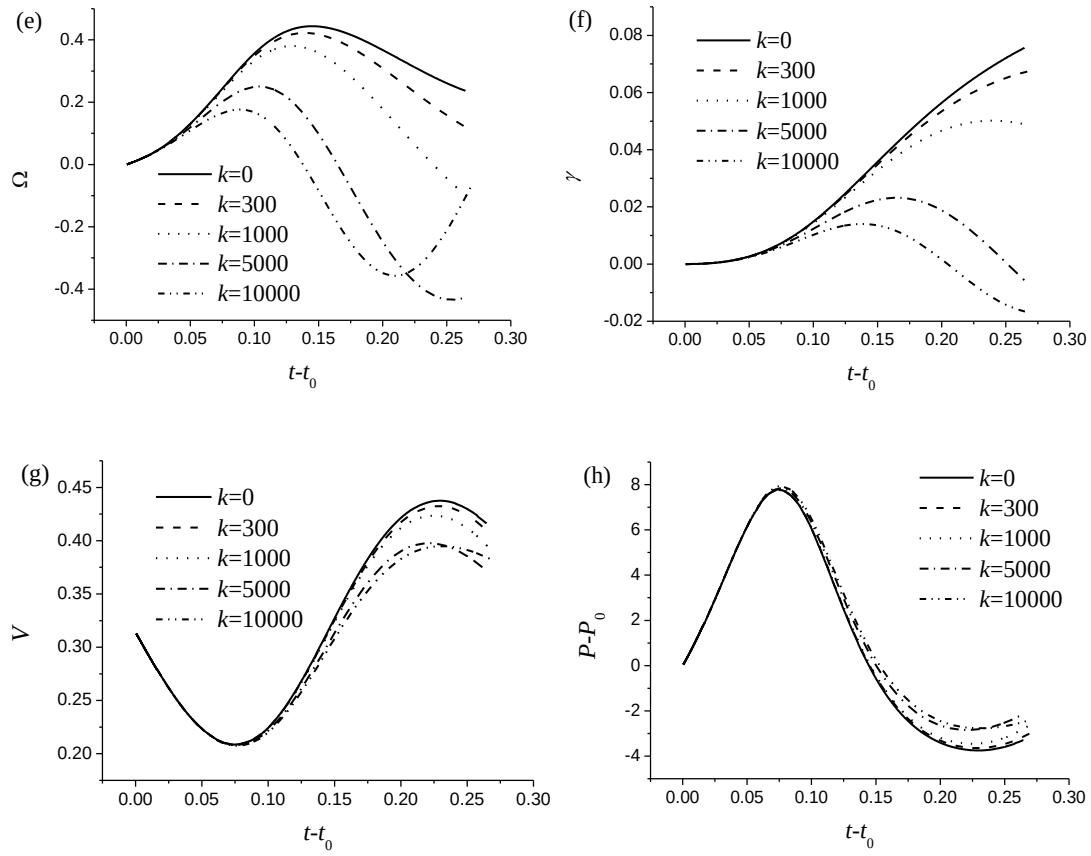

Fig. 12. The time histories of (a) horizontal velocity, (b) horizontal displacement, (c) vertical velocity, (d) vertical displacement, (e) rotational velocity, (f) rotational displacement, (g) the volume and (h) the pressure of air bubble for a TPL at different tendon stiffness.

4. Conclusions

The problem of breaking wave impacting on the floating body with air bubble effect has been modelled through the boundary element method, based on velocity potential theory with fully nonlinear boundary conditions. The dual systems and auxiliary function method are adopted to deal with the extremely small impact zone at the initial stage and decouple the mutual dependence of fluid loading, air bubble deformation and body motion, respectively. Extensive simulations have been undertaken for various cases of breaking wave impact, from which the following conclusions can be drawn.

(1) At the early stage of impact, the area of the wetted surface at the impact zone is very small while the impact pressure is very large, which is mainly due to the large relative velocity between the wave and body and the blunt shape of the wave front. After a very short impulse stage, as time increases, the impact pressure decreases rapidly.

(2) The air bubble pressure varies with its volume. When time t is not large, due to the fact that the wave front has a large plunging speed and the velocity of body is small, the air bubble volume decreases rapidly, and correspondingly, the bubble pressure increases rapidly. The increased air bubble pressure supplies a force that simultaneously accelerates the body and decelerates the fluid coming from the other side of the bubble. Consequently, the air bubble volume will increase while the pressure will decrease. It is possible that the bubble pressure will fall below the ambient pressure,

which effectively provides a suction force on the body.

(3) For the case of a floating breakwater, the horizontal direction is effectively restrained through two cables with small angles relative to the seabed, while the vertical motion is less affected. The variations of the air bubble volume and pressure are mainly due to the rotational motion of the body in addition to the wave plunging itself. When cable stiffness k is large, the horizontal, vertical and rotational displacements of the body are all related to a single parameter and the body effectively has one degree of freedom, while the former is much larger than the latter two. Different from smooth wave loading, in a breaking wave, the body will experience a large impact force and air bubble pressure force within a short period of time. For a breakwater, the momentum obtained from the breaking wave is mainly transmitted into the motion of the body in rotational degree.

(4) For a body attached to the bed by vertical cables, the heave motion is constrained. The heave motion set going by impact may have small amplitude, but it oscillates in time with high frequency. This resembles the ringing typically seen on a TPL which could oscillate at high frequency persistently after a transient wave has long past. The air bubble volume and pressure are mainly affected by the horizontal motion which is far less restrained than the vertical motion.

(5) The present work has ignored the possible ventilation and cavitation effects. As it has been found in the simulation that the pressure during the impact may be lower than the ambient pressure, air could be sucked into the fluid and additional air cavities could be formed apart from the trapped one.

In the cases considered, the smallest absolute pressure is about $6\rho gh$, which is about $6.03\times10^4 P_a$ if $h=1m$. The vapour pressure is about $2.34\times10^3 P_a$, and thus cavitation does not occur in such a case. However, cavitation can occur under other conditions, as well as ventilation. To include their effects, the model in the present work has to be refined, which forms part of our further work.

Acknowledgements

This work is supported by Lloyd's Register Foundation through the joint centre involving University College London, Shanghai Jiaotong University and Harbin Engineering University, to which the authors are most grateful. Lloyd's Register Foundation helps to protect life and property by supporting engineering-related education, public engagement, and the application of research.

This work is also supported by the National Natural Science Foundation of China (Grant No. 11472088, 51309125) and the National Natural Science Foundation of Jiangsu (BK20151327).

References

Bagnold, R.A., 1939. Interim report on wave- pressure research. In: Proceedings of the Institution of Civil Engineers 12, 201–226.

Blackmore, P.A., Hewson, P.J., 1984. Experiments on full-scale wave impact pressures. Coastal Engineering 8, 331–346.

Bredmose, H., Bullock, G.N., Hogg, A.J., 2015. Violent breaking wave impacts. Part 3. Effects of scale and aeration. Journal of Fluid Mechanics 765, 82-113.

Bullock, G.N., Crawford, A.R., Hewson, P.J., Walk-den, M.J.A., Bird, P.A.D., 2001. The influence of air and scale on wave impact pressures. Coastal Engineering 42, 291–312.

Choi, S.J., Lee, K.H., Gudmestad, O.T., 2015. The effect of dynamic amplification due to a structure's vibration on breaking wave impact. Ocean Engineering 96, 8–20.

Cointe, R., Armand, J.L., 1987. Hydrodynamic impact analysis of a cylinder. Journal of Offshore Mechanics and Arctic Engineering 109, 237 – 243.

Cooker, M.J., Peregrine, D.H., 1990. Violent water motion at breaking-wave impact. In: 22nd International Conference on Coastal Engineering 12, 164-176.

Cooker, M.J., Peregrine, D.H., 1995. Pressure–impulse theory for liquid impact problems. Journal of Fluid Mechanics 297, 193–214.

Cooker, M.J., 1996. Sudden changes in a potential flow with a free surface due to impact. The Quarterly Journal of Mechanics & Applied Mathematics 49, 581–591.

Duan, W.Y., Xu, G.D., Wu, G.X., 2009. Similarity solution of oblique impact of wedge-shaped water column on wedged coastal structures. Coastal Engineering 56, 400–407.

Hattori, M., Arami, A., Yui, T., 1994. Wave impact pressure on vertical walls under breaking waves of various types. Coastal Engineering 22, 79-114.

Hu, Z.Z., Mai, T., Greaves, D., Raby, A., 2017. Investigations of offshore breaking wave impacts on a large offshore structure. Journal of Fluids and Structures 75, 99-116.

Kamath, A., Chella, M.A., Bihs, H., Arntsen, Ø.A., 2016. Breaking wave interaction with a vertical cylinder and the effect of breaker location. Ocean Engineering 128, 105-115.

Khabakhpasheva, T.I., Wu, G.X., 2007. Coupled compressible and incompressible approach for jet impact onto elastic plate. In: Proceedings of 22th Workshop on Water Waves and Floating Bodies, Plitvice, Croatia.

Lu, C.H., He, Y.S., Wu, G.X., 2000. Coupled analysis of nonlinear intersection between fluid and structure during impact. Journal of Fluids and Structures 14, 127-146.

Ma, R.J., Li, G.X., 2002. Breaking wave forces on vertical cylinders. Journal of Hydrodynamics 14, 110-112.

Manjula, R., Sannasiraj, S.A., Saravanan, S., 2015. Experimental investigation of response of vertical slender cylinder under breaking wave impact. Aquatic Procedia 4, 227–233.

Nagai, S., 1961. Shock pressures exerted by breaking waves on breakwaters. Transactions of the American Society of Civil Engineers 126, 772-809.

Peregrine, D.H., 2003. Water-wave impact on walls. Annual Review of Fluid Mechanics 35, 23–43.

Song, B.Y., 2015. Fluid/structure impact with air cavity effect. University College London, PhD thesis.

Stanczak, G., Oumeraci, H., 2012. Modelling sea dike breaching induced by breaking wave impact-laboratory experiments and computational model. Coastal Engineering 59, 28-37.

Sun, S.L., Wu, G.X., 2013. Oblique water entry of a cone by a fully three dimensional nonlinear method. Journal of Fluids and Structures 42, 313-332.

Sun, S.Y., Sun, S.L., Wu, G.X., 2015. Oblique water entry of a wedge into waves with gravity effect. Journal of Fluids and Structures 52, 49-64.

Sun, S.L., Sun, S.Y., Wu, G.X., 2016. A three dimensional infinite wedge shaped solid block sliding into water along an inclined beach. Journal of Fluids and Structures 66, 447-461.

Tanizawa, K., Yue, D.K.P., 1992. Numerical computation of plunging wave impact loads on a vertical wall. Part 2. The air pocket. In: Proceedings of 7th International Workshop on Water Waves and Floating Bodies, Val de Reuil, France.

Wagner, H., 1932. Über Stoß-und Gleitvorgänge an der Oberfläche von Flüssigkeiten. Zeitschrift für angewandte Mathematik und Mechanic 12, 193-215.

Wu, G.X., Eatock Taylor, R., 1996. Transient motion of a floating body in steep waves. In:

Proceedings of 11th Workshop on Water Waves and Floating Bodies, Hamburg, Germany.
Wu, G.X., 1998. Hydrodynamic force on a rigid body during impact with liquid. Journal of Fluids and Structures 12, 549–559.
Wu, G.X., 2001. Initial pressure distribution due to jet impact on a rigid body. Journal of Fluids and Structures 15, 365-370.
Wu, G.X., Eatock Taylor, R., 2003. The coupled finite element and boundary element analysis of nonlinear interactions between waves and bodies. Ocean Engineering 30, 387-400.
Wu, G.X., Sun, H., He, Y.S., 2004. Numerical simulation and experimental study of water entry of a wedge in free fall motion. Journal of Fluids and Structures 19, 277-289.
Wu, G.X., 2007a. Fluid impact on a solid boundary. Journal of Fluids and Structures 23, 755–765.
Wu, G.X., 2007b. Two-dimensional liquid column and liquid droplet impact on a solid wedge. The Quarterly Journal of Mechanics and Applied Mathematics 60, 497–511.
Xu, G.D., Wu, G.X., 2013. Hydrodynamics of a submerged hydrofoil advancing in waves. Applied Ocean Research 42, 70–78.
Zhang, S., Yue, D.K.P., Tanizawa, K., 1996. Simulation of plunging wave impact on a vertical wall. Journal of Fluid Mechanics 327, 221–254.
Zhou, B.Z., Wu, G.X., 2014. Resonance of a tension leg platform exited by third-harmonic force in nonlinear regular waves. Philosophical Transactions of the Royal Society A 373, 1-20.